Tailoring of misfit along interfaces between ZnxMn3-xO4 and Ag

Mogck, S.; Kooi, B.J.; de Hosson, J.T.M.

Published in:
Acta Materialia

DOI:
10.1016/j.actamat.2004.08.042

Publication date:
2004

Available online at www.sciencedirect.com
SCIENCE DIRECT®
Acta Materialia 52 (2004) 5845–5851
Acta MATERIALIA
www.actamat-journals.com

Tailoring of misfit along interfaces between $Zn_xMn_{3-x}O_4$ and Ag

S. Mogck, B.J. Kooi, J.Th.M. De Hosson *

Department of Applied Physics, Materials Science Centre and Netherlands Institute of Metals Research, University of Groningen, Nijenborgh 4, 9747 AG Groningen, The Netherlands

Received 2 May 2004; accepted 31 August 2004
Available online 27 September 2004

Abstract

This work is aimed at examining how the tetragonality of $Zn_xMn_{3-x}O_4$ spinel structures depends on the chemical composition when $Zn_xMn_{3-x}O_4$ is embedded in a metal matrix. The paper focuses on a wide range of $Zn_xMn_{3-x}O_4$ precipitates in a Ag matrix with x varying between 0 and 1.5. This variation of x has been obtained by internal oxidation of Ag–2at.%Mn–4at.%Zn in air followed by annealing in vacuo at different temperatures. It will be demonstrated that the Zn concentration x in $Zn_xMn_{3-x}O_4$ has a major influence on the interfacial misfit and orientation relation between $Ag/Zn_xMn_{3-x}O_4$. The degree of mismatch of 10.4% of {1 1 1} Ag–Mn_3O_4 and 2.4% of Ag–$Zn_{1.5}Mn_{1.5}O_4$ was visualized using the Bragg filtering technique on HRTEM micrographs of those interfaces. It was possible to identify misfit dislocations qualitatively with this technique at {1 1 1} Ag–$Zn_xMn_{3-x}O_4$ interfaces with different degree of mismatch.

Keywords: Interfaces; Composites; High-resolution electron microscopy; Dislocation structure; Metal and alloys

1. Introduction

The present work focuses on $Zn_xMn_{3-x}O_4$ precipitates in a silver matrix with a wide variation of the zinc concentration. The misfit and orientation relation as a function of the zinc content x between Ag and $Zn_xMn_{3-x}O_4$ by means of HRTEM are scrutinized. The basic idea is to see why and how the misfit between these dissimilar materials can be tuned by varying the chemical composition.

Animoff [1] measured with X-ray powder diffraction the tetragonal distortion of Mn_3O_4. The lattice constants are $a = 5.75$ Å and $c = 9.42$ Å (SG: I4/amd). Compared to the (cubic) spinel AB_2O_4 it is more convenient to consider Mn_3O_4 with $a = 8.14$Å (i.e. $\sqrt{2}$ times 5.75 Å) and $c = 9.42$Å (SG: Fd3m), i.e. [1 0 0] and [0 1 0] in spinel correspond to [1 1 0] and $[\bar{1}\ 1\ 0]$ for I4/amd [2]. The distortion of the crystalline lattice ($c/a > 1$) arises from the presence of the Mn^{3+} on the octahedral sites of the spinel lattice [3]. An analysis of the electronic configuration of the 3d transition series shows (e.g. for Mn^{3+}, Cu^{2+}) that the doublet states cannot be degenerated in the crystal field and therefore in the case of orbital degeneracy the octahedron is deformed ($c/a > 1$). On the other hand, for the tetrahedron the deformation leads to $c/a < 1$. These deformations caused by the cooperative Jahn–Teller (JT) distortion takes the dynamic JT effect at higher temperatures into account by including anisotropic (nonlinear) JT couplings. A calculation of the tetragonal distortion in spinels was performed [4], where the molecular field treatment was applied for relative high temperatures ($T \geqslant 100$ K). The decrease of the Mn^{3+} concentration on the octahedral sites or the increase of the temperature is generally known to result in the order–disorder transition. The phase diagram ZnO/Mn_3O_4 [5] shows that the tetragonal phase is stable up

* Corresponding author. Tel.: +31 503 634 898; fax: +31 503 634 881.
E-mail address: hossonj@phys.rug.nl (J.Th.M. De Hosson).

1359-6454/$30.00
doi:10.1016/j.actamat.2004.08.042

to 1100 °C in air. Above this temperature a reversible tetragonal to cubic transition occurs. This anneals the cooperative JT distortion and the cubic structure is observed.

For zinc manganites $Zn_xMn_{3-x}O_4$ the Zn^{2+} ions have a preference to be present on the tetrahedral sites of the spinel lattice [3]. From $x = 0$ up to $x = 1.5$ the tetragonal distortion decreases gradually from $c/a = 1.16$ to $c/a = 1$ at room temperature [5]. It was shown [6] that the transition temperature from tetragonal to cubic decreases with the increase of the zinc content. For zinc concentrations $x = 1$ the Zn^{2+} cations start to exchange with the Mn^{3+} cations. This reduces the Mn^{3+} concentration on the octahedral sites of the spinel structure according to the structural formula:

$$Zn^{2+}\left(Zn_x^{2+}Mn_x^{4+}Mn_{2-2x}^{3+}\right)O_4. \quad (1)$$

This formulation indicates that the concentration of the JT ion Mn^{3+} on the octahedral sites decreases whereas the Mn^{4+} concentration increases, thereby reducing the tetragonality.

Internal oxidation of Ag–3at.%Mn resulted in octahedral shaped Mn_3O_4 precipitates due to the {1 1 1} facets inside the silver matrix [7,8]. The orientation relation between Ag and Mn_3O_4 and the dislocation structure at these metal–oxide interfaces was investigated by us in detail via HRTEM and atomistic calculations [7,8]. The tetragonal distortion leads to a configuration where only a few planes and directions of Ag and Mn_3O_4 can be parallel simultaneously whereas other planes show mutual tilting (up to 7.6° [7,8]) or both tilting and twisting. This paper concentrates how the interface structures can be tailored by varying the chemical composition of $Zn_xMn_{3-x}O_4$ spinel structures in Ag.

2. Experimental details

A silver alloy containing 2 atomic percent (at.%) Mn was made in a high-frequency furnace by melting the pure components (Purity 99.99% by weight) in one aluminum crucible under argon protective oxygen free atmosphere. The silver alloy was cold rolled down to 100 μm and homogenized in an evacuated quartz tube for one week at 700 °C. During the homogenization process a piece corresponding to 4 at.% Zn was positioned separately in the evacuated quartz tube and dissolved into the silver alloy. Oxide precipitates in the silver matrix were obtained by oxidation of the alloy in air. Five different sample systems with different oxidations and annealing steps of Ag–2at.%Mn–4at.%Zn were fabricated, as follows:

1. Internal oxidation in air at 900 °C for 1/2 h.
2. Internal oxidation in air at 800 °C for 5 h.
3. Internal oxidation in air at 900 °C for 1/2 h and annealing in vacuum at 900 °C for 5 h.
4. Internal oxidation in air at 800 °C for 5 h and annealing in vacuum at 800 °C for 24 h.
5. Internal oxidation in air at 800 °C for 5 h, annealing in vacuum at 800 °C for 24 h and re-internal oxidation in air at 900 °C for 1/2 h.

TEM samples were prepared by grinding, dimpling and ion milling 3 mm discs to electron transparency. HRTEM imaging was performed with a JEOL 4000 EX/II, operating at 400 kV (spherical aberration coefficient: 0.97 ± 0.02, spread of defocus: 7.8 ± 1.4 nm, beam semi-convergence angle: 0.8 mrad). The HRTEM micrographs were obtained from digitized negatives. EDX measurements were carried out using a JEOL 2010 F operating at 200 kV with a probe-size of about 1 nm (FWHM). Each measured composition of precipitates was determined by averaging over about 15 EDX measurements. HRTEM image simulation was performed with MacTempas (supported by CrystalKit).

3. Results

Table 1 gives an overview over the different measured compositions after oxidizing in air and annealing in vacuo of Ag–2at.%Mn–4at.%Zn. Internal oxidation at 900 and 800 °C (1/2 and 5 h, respectively) results according to the EDX measurements and HRTEM images in octahedral shaped $Zn_{1.5}Mn_{1.5}O_4$ precipitates (cubic spinel Fd3m [2]). A HRTEM image of a $Zn_{1.5}Mn_{1.5}O_4$ precipitate with a size of approximately 5 nm is shown in Fig. 1. After internal oxidation in air at 900 and 800 °C the samples were annealed at the same temperature in vacuo for 5 and 24 h, respectively. The cubic spinel phase $Zn_{1.5}Mn_{1.5}O_4$ decomposes into two different types of oxide precipitates. The treatment at 900 °C results in small elongated octahedral shaped $Zn_{0.56}Mn_{2.44}O_4$ (tetragonally distorted spinel) precipitates (Fig. 3(left)) and approximately 2–10 times longer plate-shaped precipitates of $Zn_{0.93}Mn_{0.07}O$ (Fig. 2). Basically, the plate precipitates have a hexagonal wurtzite structure, but in many cases HRTEM images show that strong stacking disorder of the basal planes is present locally leading to the fcc based sphalerite stacking (Fig. 3(right)). Annealing at 800 °C in vacuo also leads to plate-like $Zn_xMn_{1-x}O$, but with a lower Zn concentration of $x = 0.88$. On the other hand, the spinel phase of $Zn_xMn_{3-x}O_4$ is not present. In contrast, after this annealing at 800 and 900 °C small inclusions with a maximum size of 5 nm are present in the silver matrix, as seen in Fig. 2. Analytical TEM reveals that these inclusions are fcc phase $Mn_{0.86}Zn_{0.14}O$ (i.e have the rocksalt structure).

Table 1
Characterization in concentration x, shape, size and crystallographic structure of the formed $Zn_xMn_{3-x}O_4$ precipitates for different oxidation and annealing steps of Ag–2at.%Mn–4at.%Zn

Ag–2at.%Mn–4at.% Zn	Phase of the precipitates	Zn concentration	Shape of the precipitates	Dimension of the precipitates
Oxidation at 900 °C for 1/2 h in air	$Zn_xMn_{3-x}O_4$ (SG: Fd3m)	$x = 1.5 \pm 0.1$	Octahedrally shaped precipitates bounded by {1 1 1} planes in Ag	5–15 nm
Oxidation at 800 °C for 5 h in air	$Zn_xMn_{3-x}O_4$ (SG: Fd3m)	$x = 1.5 \pm 0.1$	Octahedrally shaped precipitates	5–15 nm
Oxidation at 900 °C for 1/2 h in air + annealing in vacuo at 900 °C for 5 h	$Zn_xMn_{3-x}O_4$ (SG: I4/amd) wurtzite/sphalerite	x = 0.56 ± 0.1	Elongated -and octahedrally shaped	Length: 10–25 nm, width: 5–10 nm
	$Zn_xMn_{1-x}O$ (SG : $P6_{3mc}/F\bar{4}3m$)	$x = 0.93 \pm 0.03$	$Zn_xMn_{3-x}O_4$ plate like/ truncated trigonal shaped $Zn_xMn_{1-x}O$	Length: 50–120 nm, width: 8–25 nm
Oxidation at 800 °C for 5 h in air + annealing in vacuo at 800 °C for 24 h	$Zn_xMn_{1-x}O$ fcc (SG: Fm3m) wurtzite/sphalerite	$x = 0.15 \pm 0.04$	Octahedrally shaped $Mn_xZn_{1-x}O$ plate like/	5–10 nm
	$Zn_xMn_{1-x}O$ (SG : $P6_{3mc}/F\bar{4}3m$)	$x = 0.88 \pm 0.05$	truncated trigonal shaped $Zn_xMn_{1-x}O$	Length: 50–100 nm, width: 10–15 nm
Oxidation at 800 °C for 5 h in air + annealing in vacuo at 800 °C for 24 h + oxidation in air at 900 °C for 1/2 h	$Zn_xMn_{3-x}O_4$ (SG: I4/amd) wurtzite/sphalerite	$x = 1.03 \pm 0.14$	Octahedrally shaped $Zn_xMn_{3-x}O_4$ plate like/	5–10 nm
	$Zn_xMn_{1-x}O$ (SG : $P6_{3mc}/F\bar{4}3m$) and $Zn_xMn_{3-x}O_4$/Zn(Mn)O	$x = 0.96 \pm 0.02$	truncated trigonal shaped $Zn_xMn_{1-x}O$, $Zn_xMn_{3-x}O_4$/	Length: 50–100 nm, width: 10–15 nm
		$x = 1.47 \pm 0.02$	$Zn_xMn_{1-x}O$	Length: 30–40 nm, width: 10–15 nm

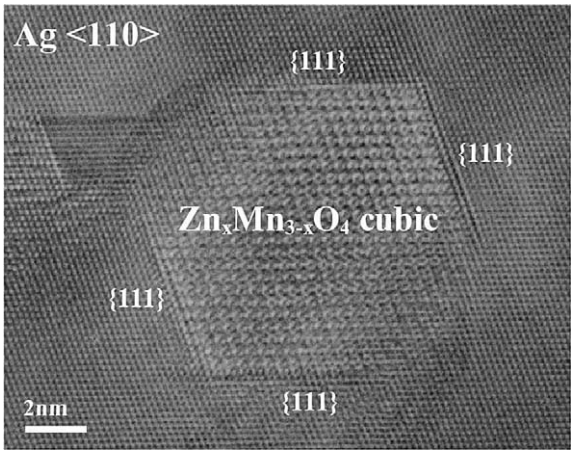

Fig. 1. Internal oxidation of Ag–2at.%Mn–4at.%Zn in air at 900 °C for 1/2 h results in octahedral shaped precipitates bounded by {1 1 1} planes with a size of 5–10 nm in silver matrix. Energy dispersive measurements reveal cubic spinel phased $Zn_{1.55}Mn_{1.45}O_4$. The TEM micrograph shows such a precipitate in the ⟨1 1 0⟩ viewing direction. It is observable that all four interfacial {1 1 1} planes between precipitate and matrix are simultaneously parallel.

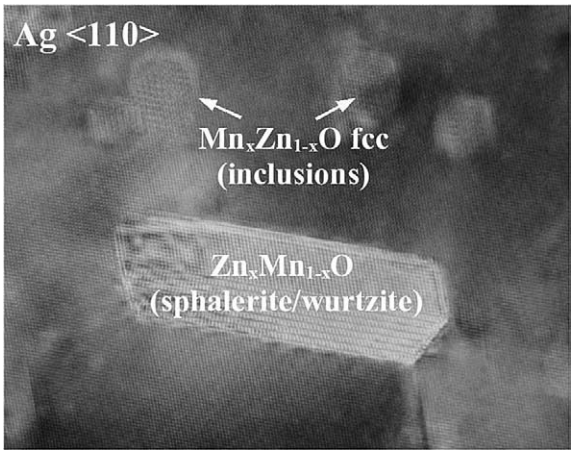

Fig. 2. Plate-shaped precipitate of $Zn_{0.98}Mn_{0.02}O$ after internal oxidation at 900 °C for 1/2 and annealing in vacuo at 900 °C for 5 h.

After re-internal oxidation, the inclusions transfer back to octahedral shaped $Zn_{1.04}Mn_{1.96}O_4$ with a size of 5–10 nm. In the plate-like precipitates the Zn concentration increases from $x = 0.88$ to $x = 0.96$. So, compared to the first internal oxidation treatment with only $Zn_{1.5}Mn_{1.5}O_4$ precipitates, after re-oxidation a kind of phase separation into $ZnMn_2O_4$ and ZnO has occurred. Coupled to this picture, some plate-like precipitates are visible that split into two phases: cubic spinel phase $Zn_{1.47}Mn_{1.53}O_4$ directly connected to the ZnO-based wurtzite/sphalerite structure (Fig. 3(right)). Besides these plate-like precipitates also wurtzite and sphalerite $Zn_xMn_{1-x}O$ forms into truncated trigonal shaped precipitates as could be observed in some cases after annealing at 900 and 800 °C. Detailed observations of ZnO precipitates with wurtzite and sphalerite structure in Ag and Pd have been published earlier [9,10]. In the following, only the spinel phased precipitates will be considered.

The mismatch between $Zn_xMn_{3-x}O_4$ and Ag changes by varying the concentration x. The lattice parameter and degree of tetragonal distortion for different Zn concentrations of $Zn_xMn_{3-x}O_4$ was given in [5]. The OR between the octahedral shaped $Zn_{1.5}Mn_{1.5}O_4$ and the Ag matrix (Fig. 1) can be regarded as parallel topotaxy (cube-on-cube) where the interfaces are formed by the parallel {1 1 1} of metal and oxide. In contrast, due to the tetragonality of $Zn_{0.56}Mn_{2.44}O_4$, as shown in

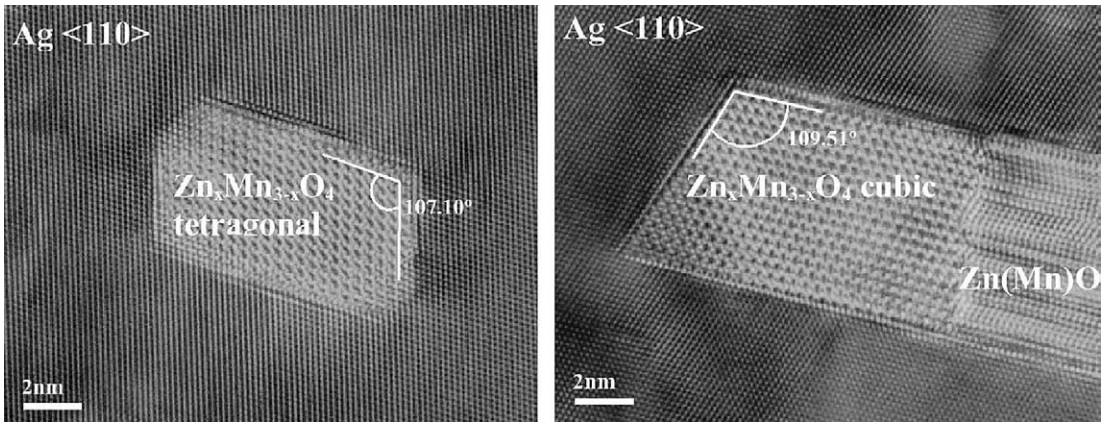

Fig. 3. (left) HRTEM image showing an elongated octahedral $Zn_{0.54}Mn_{2.46}O_4$ in the ⟨1 1 0⟩ viewing direction of an internal oxidized Ag–2at.%Mn–4at.%Zn (900 °C for 1/2 h) annealed at 900 °C for 5 h in vacuo. (right) HRTEM image showing a precipitate where cubic spinel $Zn_{1.47}Mn_{1.53}O_4$ is connected to wurtzite/sphalerite $Zn_{0.96}Mn_{0.04}O$. These precipitates grow after internal oxidation at 900 °C for 1/2 h of a sample that was previously annealed in vacuo, see Table 1.

Fig. 3(left), with *a*-axis of 0.808 nm and *c*-axis of 0.920 nm only one or two direction and planes can be simultaneously parallel. For viewing the interface between the $Zn_xMn_{3-x}O_4$ and the Ag matrix, the Ag crystal is tilted into the ⟨1 1 0⟩ zone axis. The tetragonality of $Zn_xMn_{3-x}O_4$ can easily be observed in HRTEM images (using the Ag crystal as reference), because of the difference between the *c*-and *a*-axes. The tetragonality can be detected by measuring the blunt angle between {1 1 1} planes of the precipitate: {1 1 1} planes of a cubic crystal such as Ag make a blunt angle of 109.5° in all possible ⟨1 1 0⟩ projections. For tetragonal distorted spinel, however, in the [1 1 0] viewing direction an angle larger than 109.5° is observed (with 1/3 probability) and in the [1 0 1] and [0 1 1] directions less than 109.5° is observed (with 2/3 probability). Fig. 4 depicts the blunt angle between {1 1 1} planes of $Zn_xMn_{3-x}O_4$ when viewed along [1 1 0] or [1 0 1]/[0 1 1] for different Zn concentrations *x* based on the lattice constants given in [5].

The calculated misfit between $Zn_xMn_{3-x}O_4$ and Ag at parallel {1 1 1} interfaces along [1 1 2] varies from 10.4% ($x = 0$) to 2.4% ($x = 1.5$) based on the *a* and *c* lattice constant [5], as seen in Fig. 4. Note that the mis-

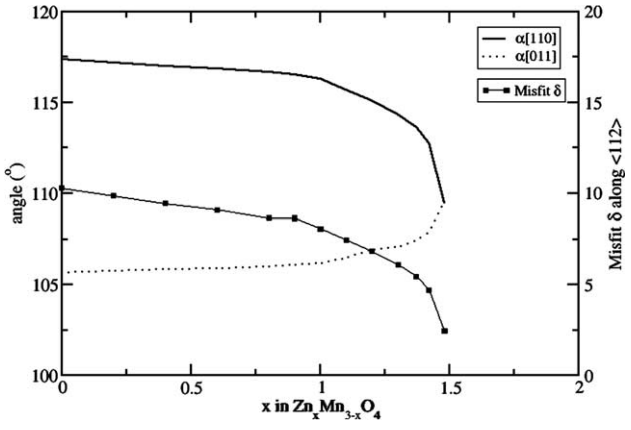

Fig. 4. Angle between {1 1 1} planes of octahedral $Zn_xMn_{3-x}MnO_4$ by variation of zinc concentration *x*. See angles in Fig. 3. Misfit at {1 1 1} Ag–$Zn_xMn_{3-x}O_4$ interfaces along ⟨1 1 2⟩ decrease by increasing the amount of *x* in $Zn_xMn_{3-x}O_4$ because the *c*/*a* ratio decreases.

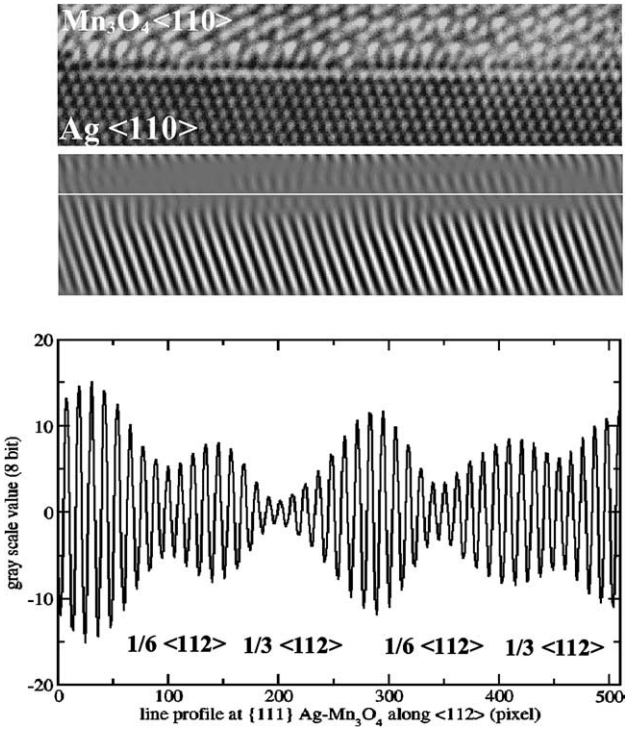

Fig. 5. Visualization of the mismatch between Ag and Mn_3O_4. Top panel shows the HRTEM image of an {1 1 1} Ag–Mn_3O_4 interface. The middle panel shows the inverse FFT of the Bragg filtered {1 1 1} spots of the HRTEM image. The white line along the Ag–Mn_3O_4 interface (middle panel) indicates the line profile of the {1 1 1} Ag–Mn_3O_4 interface, as seen in the bottom panel. The minima in the line profile correspond directly to the misfit between Ag and Mn_3O_4.

match in the perpendicular [1 $\bar{1}$ 0] direction varies from −0.4% ($x = 0$) to +2.4% ($x = 1.5$).

Using HRTEM images of {1 1 1} heterophase interfaces the misfit between metal and oxide can be directly observed with Bragg filtering of {1 1 1} planes. This is demonstrated in Figs. 5 and 6. The modulation of the line profiles in Figs. 5 and 6 corresponds to the mismatch of 10.4% and 2.4% (approx. 11 periods in the metal vs. 10 periods in the oxide and 42 periods in the metal vs. 41 in the oxide, respectively) in the {1 1 1} lattice fringes at Ag–$Zn_xMn_{3-x}O_4$ with $x = 0$ and $x = 1.5$, respectively (Figs. 5 and 6). The line profile of the Ag–Mn_3O_4 interface (Fig. 5) shows that the magnitude of the intensity modulation reveals the possibility to distinguish between the Burgers vectors of type 1/3 ⟨1 1 2⟩ and 1/6 ⟨1 1 2⟩ that were observed and calculated to be present along the Ag–Mn_3O_4 interface [7,8]. This different degree of modulation results from the undulation of the outmost Ag monolayer at the interface [7,8]. The 1/3 ⟨1 1 2⟩ Burgers vector corresponds to a stronger lattice distortion than the 1/6 ⟨1 1 2⟩. However, for the line profile seen in Fig. 6 bottom panel of the {1 1 1} Ag–$Zn_{1.5}Mn_{1.5}O_4$ interface the modulation intensity cannot be unambiguously interpreted, because of the two-dimensional network of misfit dislocations present at the interface. I.e. the mismatch of 2.4% is present along all directions whereas at the Ag–Mn_3O_4 interface a more or less one-dimensional mismatch occurs, where the misfit dislocations can be observed end-on.

The degree of modulation can be directly confirmed with simulated HRTEM images of relaxed {1 1 1} Ag–Mn_3O_4 interfaces, as seen in Fig. 7. The calculation of the relaxed atomic configuration of the Ag atoms at the {1 1 1} Ag–Mn_3O_4 interface was obtained by the program described in [11] and is fully discussed in [7,8]. Inverse FFT on Bragg filtered {1 1 1} spots make it possible to distinguish between the Burgers vectors of type 1/3 ⟨1 1 2⟩ and 1/6 ⟨1 1 2⟩ (Fig. 7, bottom panel), however for the disregistry where the misfit dislocation at Ag–Mn_3O_4 interfaces

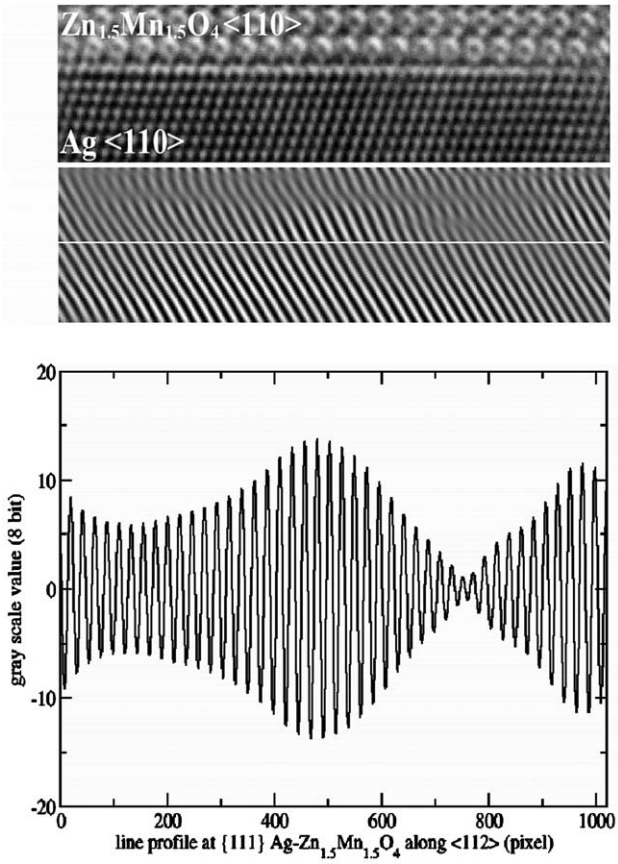

Fig. 6. Visualization of the mismatch between Ag and $Zn_{1.5}Mn_{1.5}O_4$. Top panel shows the HRTEM image of an {1 1 1} Ag–$Zn_{1.5}Mn_{1.5}O_4$ interface. The middle panel shows the inverse FFT of the Bragg filtered {1 1 1} spots of the HRTEM image. The white line along the Ag–$Zn_{1.5}Mn_{1.5}O_4$ interface (middle panel) indicates the line profile of the {1 1 1} Ag–$Zn_{1.5}Mn_{1.5}O_4$ interface, as seen in the bottom panel. The minima in the line profile correspond directly to the misfit between Ag and $Zn_{1.5}Mn_{1.5}O_4$.

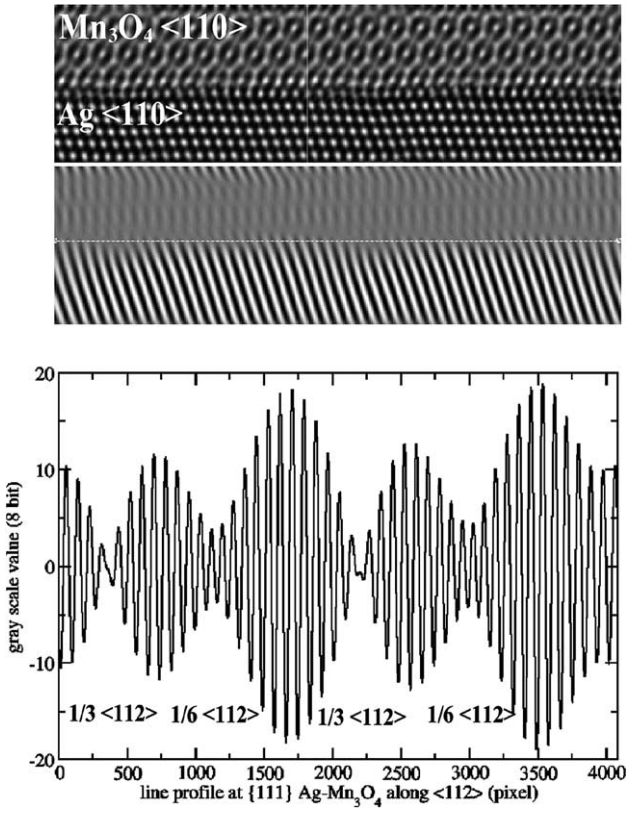

Fig. 7. Visualization of the mismatch between Ag and Mn_3O_4. Top panel shows the HRTEM image simulation of an relaxed 1 1 1 Ag–Mn_3O_4 interface (defocus −6 nm, thickness 4 nm, beam tilt of 1.3 mrad[1]). The middle panel shows the inverse FFT of the Bragg filtered {1 1 1} spots of the simulated HRTEM image. The white line along the Ag–Mn_3O_4 interface (middle panel) indicates the line profile of the {1 1 1} Ag–Mn_3O_4 interface, as seen in the bottom panel. The variations of the intensity modulation in the line profile correspond directly to the misfit dislocation between Ag and Mn_3O_4.

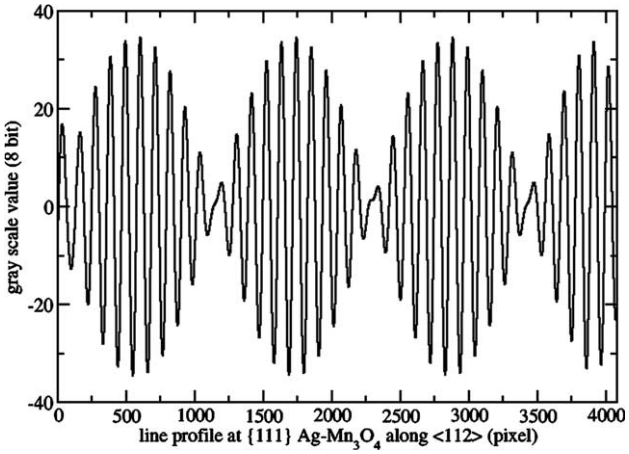

Fig. 8. Visualization of the mismatch between Ag and Mn_3O_4. The line profile shows the HRTEM image simulation of an unrelaxed {1 1 1} Ag–Mn_3O_4 interface (defocus −6 nm, thickness 4 nm, beam tilt of 1.3 mrad[1]). The mismatch of 10.0% between Ag and Mn_3O_4 is visible, but without any misfit dislocation, as seen in Fig. 4.

is exactly located, additional determination of the position of the Ag atoms and the position of the oxygen atoms along the interface must be performed in real space, as described in [7,8].

In contrast, inverse FFT on Bragg filtered {1 1 1} spots on unrelaxed {1 1 1} HRTEM simulated Ag–Mn_3O_4 interfaces show constant degree of modulation in the line profiles, as see in Fig. 8. Thus, comparing Figs. 5, 7 and 8 clearly indicates that {1 1 1} Ag–Mn_3O_4 is a semi-coherent and not an incoherent interface.

4. Discussion

The direct nucleation of Mn_3O_4 in Ag compared with the presence of MnO precipitates in Cu is probably caused by the different partial pressure of oxygen during oxidation of Ag and Cu. Ag is oxidized in air, whereas Cu is oxidized as the partial pressure pertaining to the equilibrium between Cu/Cu_2O (powder). Another possible explanation is the difference of the oxygen permeability through Ag and Cu. At 900 °C c_0D_0, with c_0 the oxygen solubility and D_0 the diffusion coefficient of oxygen within the matrix, is about two orders of magnitude larger in Ag than in Cu [12]. The presence of Zn and Mn in the silver matrix results after internal oxidation at 900 and 800 °C in cubic $Zn_{1.5}Mn_{1.5}O_4$ octahedrally shaped precipitates. The main reason for this cubic spinel is likely to be the similar diffusion constants of Mn and Zn ($D_{Mn} = 7.92 \times 10^{-9}$ cm^2/s (at 900 °C) [13] and $D_{Zn} = 8 \times 10^{-9}$ cm^2/s (at 900 °C) [14]) and after the oxidation front during the oxidation process the same amount of Zn and Mn are present when the precipitates grow. After annealing in vacuo the $Zn_{1.5}Mn_{1.5}O_4$ octahedrally shaped precipitates decompose to MnO and ZnO precipitates. From thermodynamic point of view the change of the Gibbs-free energy for the bulk oxidation of Mn into several oxide phases is different if the Mn concentration is limited or the O concentration is limited. In the first case the calculation based on the Gibbs-free energy per Mn (atom or mole) [15] shows that Mn_3O_4 precipitates are thermodynamically preferred, whereas in the second case the calculation of the Gibbs-free energy per O (atom or mole) reveals that MnO precipitates are favored [15]. The same applies here. After internal oxidation, where sufficient oxygen is available and the amount of Mn and Zn is limited $Zn_{1.5}Mn_{1.5}O_4$ is favored. On the other hand, during annealing in vacuo the amount of oxygen is limited and decomposition in the more stable MnO and ZnO phases occurs. At 900 °C decomposition can occur much faster than at 800 °C. This is probably the reason that the Mn concentration found within the ZnO precipitates is still higher at 800 °C than at 900 °C. However, at 900 °C also a small amount (about 2%) of elongated octahedral shaped $Zn_{0.56}Mn_{2.44}O_4$ (tetragonally distorted) precipitates is present. The partial oxygen pressure can be high enough after internal oxidation at 900 °C. The oxygen dissolution in Ag at 900 °C is almost two orders of magnitude higher than at 800 °C [17]. This higher oxygen content after a heat treatment at 900 °C is the reason that after annealing in vacuo the spinel phase develops, because of the sufficient amount of oxygen present in the Ag matrix. After re-internal oxidation the MnO inclusion transfer to $Zn_{1.03}Mn_{1.97}O_4$ octahedrally shaped precipitates. Usually the well-defined compound $ZnMn_2O_4$ is obtained at 900 °C after long annealing time [16]. In thermal equilibrium (T = 900 °C) $Zn_xMn_{3-x}O_4$ has a low zinc content of $x < 1.08$ [16]. For higher zinc content ($x > 1.08$) the cubic phase $ZnMnO_3$ is observed [16], in addition to the spinel phase, in agreement with our observations.

5. Conclusions

The transformation from tetragonally distorted to cubic $Zn_xMn_{3-x}O_4$ (from $x = 0$ to $x = 1.5$) formed inside the silver matrix was studied. The main result shown is that it is possible to vary the Zn content x in $Zn_xMn_{3-x}O_4$ precipitates in Ag matrix by applying several oxidation and annealing steps. Atomic scale studies of the mismatch and misorientation of {1 1 1} Ag–$Zn_xMn_{3-x}O_4$ interfaces reveal clearly the decreasing misfit between Ag and $Zn_xMn_{3-x}O_4$ with increasing amount of zinc in the spinel phase. Bragg filtering is a simple method to visualize the misfit and misfit dislocations at {1 1 1} Ag–$Zn_xMn_{3-x}O_4$ interfaces and therefore to get qualitative information about the bond strength present along the semi-coherent metal–oxide interfaces [7,11].

Acknowledgement

The work is part of the research program of the Foundation of Fundamental Research on Matter (FOM-Utrecht) and has been made possible by financial support form the Netherlands Organization for Research (NWO-The Hague) and the Netherlands Institute for Metals Research.

References

[1] Animoff G. Z Krist 1926;64:475.
[2] Wyckoff RWG. Crystal structures. 2nd ed. New York: Interscience Publishers; 1963.
[3] Navrotsky A, Kleppa OJ. Inorg Nucl Chem 1967;29:2701.
[4] Englman R, Halperin B. Phys Rev B 1970;2:75.
[5] Driessens FCM, Rieck GD. J Inorg Nucl Chem 1966;28:1593.
[6] Rosenberg M, Nicolau P, Manaila R, Pausescu P. J Phys Chem Solids 1963;24:1419.
[7] De Hosson JTM, Kooi BJ. In: Nalwa HS, editor. Handbook of surfaces and interfaces in materials, vol. 1. New York: Academic Press; 2001. p. 1–114.
[8] Kooi BJ, Groen HB, De Hosson JTM. Acta Mater 1997;45:3607.
[9] Vellinga WP, De Hosson JTM. Acta Mater 1997;45:933.
[10] Groen HB, De Hosson JTM. Scr Mater 1998;38:769.
[11] Vellinga WP, De Hosson JTM, Vitek V. Acta Mater 1997;45:1525.
[12] Meijering JL. In: Herman H, editor. Advances in materials research. New York: Wiley–Interscience; 1971.
[13] Makuta F, Lijima Y, Hirano K. Trans Japan Inst Met 1979;20:551.
[14] Rothman SJ, Peterson NL. Phys Rev 1967;54:552.
[15] Kooi BJ, De Hosson JTM. Acta Mater 1998;46:1909.
[16] Guillemet-Fritsch S, Chanel C, Sarrias J, Bayonne S, Rousset A, Alcobe X, et al. Solid State Ionics 2000;128:233.
[17] Ramanarayanan TA, Rapp RA. Metall Trans 1972;3:3239.